ORIGINAL PAPER

Effect of co-precipitation and solid-state reaction synthesis methods on lithium-rich cathodes $Li_{1.2}Ni_{0.2}Mn_{0.6}O_2$

Augusto Rodriguez[1] · Miguel A. Sanservino[1] · Sofía Gómez[1] · Mariela Ortiz[1,2] · Jorge E. Thomas[3] · Arnaldo Visintin[1]

Abstract

Lithium-rich oxides ($Li_{1.2}Ni_{0.2}Mn_{0.6}O_2$) were obtained by two synthesis routes: co-precipitation method and solid-state reaction. Both materials showed a high degree of crystallinity, and XRD analysis revealed intense and well-defined signals corresponding to the R3m and C2/m space groups of these types of compounds, with a difference in the cationic order in the hexagonal structure layers. The cycling performances showed an initial discharge capacity of 200 mAh g^{-1} from the co-precipitated material, against the 150 mAh g^{-1} obtained from the solid-state reaction route but, unlike the large drop in the discharge capacity of the co-precipitated material after 160 cycles, the material obtained by solid-state reaction provided a slightly constant discharge capacity of ~120 mAh g^{-1} throughout cycling. The high initial discharge capacity of the co-precipitated material may be associated with the activation of the Li_2MnO_3 phase cycled at 0.2 C between 2.0–4.8 V and 2.0–5.2 V, the better cationic order and wider space between the layers of the $LiMO_2$ phase. Therefore, the electrochemical performance could be directly related to those structural characteristics obtained thorough the selected synthetic procedures.

Keywords Lithium-ion battery · Cathode · Lithium-rich oxides · $Li_{1.2}Ni_{0.2}Mn_{0.6}O_2$ · Synthesis method · Electrochemical performance

Introduction

The fast development of modern technology has created a wide market for new and more efficient energy storing devices that meet the electric requirements of a vast range of appliances, from cell phones to electric cars. Among those energy storing devices, Li-ion batteries play an important role in the present and future of the technological industry due to their high specific energy, high efficiency, and long life [1–3]. These characteristics are the main reasons of their extensive application in day-to-day gadgets such as cell phones and portable computers [4]. Furthermore, Li-ion batteries are expected to be used massively to store, in the form of chemical energy, electric energy coming from renewable sources [5].

Great efforts have been made to develop new types of cathode materials for Li-ion batteries, each one with their own limitations. The most common of these materials is $LiCoO_2$ that, despite having a theoretical capacity of 274 mAh g^{-1}, only exhibits a practical capacity of around 165 mAh g^{-1} [6] since not all the Li^+ can be extracted from its structure. That is why a new family of compounds, known as lithium-rich oxides, represents the perfect candidate for a new generation of cathode materials in Li-ion batteries. These oxides are usually described with the formula xLi_2MnO_3 $(1-x)LiMO_2$ with M = Ni, Co, and Mn ($0 < x < 1$) and exhibit an available capacity of 250–350 mAh g^{-1} [7–9].

Nonetheless, researchers are still facing major challenges to use these types of oxides to create an efficient and long-life battery, due to their poor rate capabilities, high initial irreversibility, poor initial coulomb efficiency, and a continuous decrease of the discharge voltage plateau. Several

✉ Sofía Gómez
sofia.gomez@ing.unlp.edu.ar

1   Instituto de Investigaciones Fisicoquímicas Teóricas y Aplicadas (INIFTA), Facultad de Ciencias Exactas (UNLP), CONICET, Diag. 113 y 64, La Plata, Argentina

2   Centro de Investigación y Desarrollo en Ciencia y Tecnología de Materiales (CITEMA), Universidad Tecnológica Nacional - CICPBA, 60 y 124, 1923 Berisso, Argentina

3   YPF Tecnología S.A, Av. del Petróleo Argentino S/N (entre 129 y 143), B1923 Berisso, Buenos Aires, Argentina

attempts have been made to improve these deficiencies, through doping with different chemical elements and quantities of the transition metals [10–14]. Furthermore, there is still no definitive theory that could explain the high discharge capacities from these materials, since several articles have reported lithium-rich compounds with discharge capacities higher than the theoretical values [15, 16].

In this work, we study the effect of two different synthesis methods on the structural and electrochemical properties of a lithium-rich oxide, $Li_{1.2}Ni_{0.2}Mn_{0.6}O_2$, in order to determine which attribute is responsible for the improvement of the electrochemical discharge capacity and stability. In addition, the obtained results could help identify which synthesis method represents a better candidate for a future large-scale production of cathode material.

Materials and methods

Preparation of Li-rich materials ($Li_{1.2}Ni_{0.2}Mn_{0.6}O_2$)

$Li_{1.2}Ni_{0.2}Mn_{0.6}O_2$ was synthesized by two different routes: co-precipitation method [17] and solid-state reaction route [18]. For the co-precipitation method, stoichiometric amounts of the transition metal acetates were dissolved in distilled water. Then, the solutions were added dropwise to a 0.1 M NaOH solution to obtain $Ni_{0.25}Mn_{0.75}(OH)_2$. This precipitate was mixed with a certain amount of Li_2CO_3 and heated in a tubular furnace with oxygen flow in two steps, first at 500 °C for 5 h and then at 850 °C for 12 h. The obtained sample was named as LiR-copp. Also, $Li_{1.2}Ni_{0.2}Mn_{0.6}O_2$ was synthesized by a solid-state reaction. Stoichiometric amounts of $Ni(OH)_2$, $MnCO_3$, and Li_2CO_3 were mixed in a planetary ball mill for 1 h at 600 rpm. The mixture was then heated in a tubular furnace under oxygen flow at 950 °C for 15 h. This material was named as LiR-SSR.

Physical characterization

The crystallographic structures of materials were determined by X-ray diffraction in a Philips-APD PW 1710 diffractometer with Cu Kα (1.542 Å) radiation in the range between 10 and 80° (2θ), with a step of 0.1° and quantified by Rietveld method. Surface characterization was carried out by Fourier transform infrared (FTIR) spectroscopy with a Thermo Scientific Nicolet iS5 using an attenuated total reflectance (ATR) accessory with a diamond window where the samples were directly pressed, in the wavenumber range 500–4000 cm^{-1} at room temperature. Scanning electron microscopy (SEM) and energy dispersive spectroscopy (EDS) were performed in a FEI scanning electron microscope. Post cycling analysis was performed disassembling the cycled cells inside the glove box.

Electrochemical characterization

The working electrodes were obtained by preparing the slurries with the following mass fraction: 80% of the electroactive lithium-rich materials, 10% of Super P carbon, and 10% of polyvinylidene fluoride (PVDF) dissolved in N-methyl-2-pyrrolidone (NMP). The suspension was coated on aluminum foil and was dried at 80 °C until the complete evaporation of NMP. Finally, 12-mm diameter electrodes were cut.

The electrochemical experiments were carried out in Swagelok T cells, assembled in an M-Braun argon-filled glove box. Lithium foil was used as counter and reference electrodes. A glass microfiber membrane was used as separator, and the 1 M solution of lithium hexafluorophosphate ($LiPF_6$) dissolved in a 1:1 w/w mixture of ethylene carbonate (EC) and imethyl carbonate (DMC) as the electrolyte.

Cyclic voltammetry (CV) was measured on a Gamry Reference 3000 potentiostat at a scan rate of 0.1 mVs^{-1} in potential ranges of 2–4.8 V and 2–5.2 V. Electrochemical impedance spectroscopy (EIS) was also performed on the above Gamry instrument in the frequency range of 10 to 1 mHz. Galvanostatic charge–discharge cycling was carried out on an Arbin multichannel potentiostat/galvanostat (MSTAT4) in the ranges of 2–4.8 V and 2–5.2 V vs. Li$^+$/Li, at different current densities (C rates).

Results and discussion

XRD analysis

Diffraction patterns of the materials obtained by co-precipitation and solid-state reaction methods are shown in Fig. 1. In both diffraction patterns, a set of intense and narrow peaks is attributable to the $LiMO_2$ laminar phase with R3m space group, beside a set of less intense peaks from the Li_2MnO_3 phase with C2/m space group. These signals are typical of Li-rich materials with good crystallinity and are well-identified for the family of lithium-rich mixed oxides [19, 20]. The clear and high definition of the (006)/(012) and (108)/(110) peaks shows that both materials possess a well-organized layered structure [21, 22].

A slight (003) peak diffraction shift towards lower angles can be observed from 18.90 to 18.80° for LiR-coop samples. This shift could indicate the bigger interplanar distance for the first compound, which could facilitate the process of Li$^+$ intercalation/deintercalation [23].

The intensity ratio $I_{(003)}/I_{(104)}$ is an important parameter of the quality of the cationic order in these layered materials [24], since it is known that Ni^{+2} cations may occupy Li$^+$ sites in the Li$^+$ layers forming barriers for Li$^+$ diffusion [25]. For the material obtained by solid-state reaction, the $I_{(003)}/I_{(104)}$ ratio is 1.18, while for the co-precipitation material, it is 1.45, indicating that the co-precipitation route generates samples
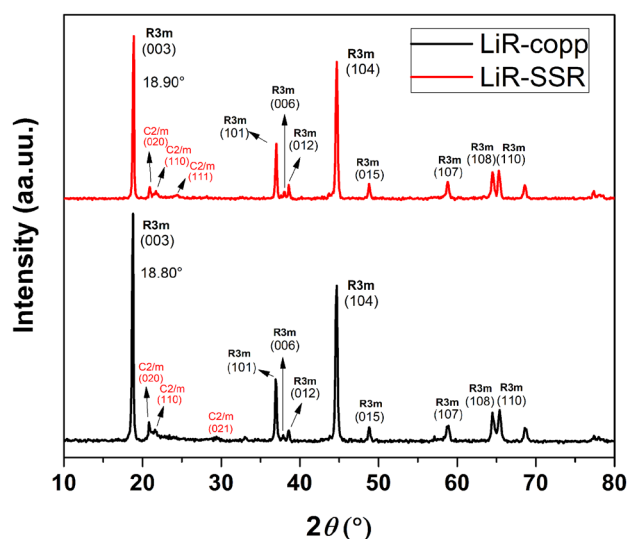
Fig. 1 Powder X-ray diffraction patterns of materials obtained by co-precipitation (LiR-copp) and solid-state reaction (LiR-SSR)

with a better cationic order in the hexagonal structure layers than the solid-state synthesis route. In addition, the intensity ratio $(I_{(006)} + I_{(012)})/(I_{(101)})$ is also related to the hexagonal ordering in the structure, and a lower ratio indicates less cation mixing [26]; this ratio value for LiR-copp material is 0.36 against 0.56 for the LiR-SSR compound, which again indicates a better cationic order for the LiR-copp. Table 1 shows the values of the lattice parameters obtained for both materials through the Rietveld refinement. It can be seen that the c/a parameters are located above 4.90 which exhibit the deviation of a disordered rock salt structure [27]. The a and c parameters, individually, are in good agreement with the lattice parameters for similar materials reported in the available literature [28]. The LiR-SSR shows higher a and c values which could be associated with the presence of greater amount of Mn^{+3} (with a higher ionic radius, 0.58 Å) that was not fully oxidized to Mn^{+4} during calcination [28].

SEM and EDS characterization

SEM images of LiR-SSR and LiR-copp materials are shown in Fig. 2. Both samples exhibit agglomerates with a homogeneous particle-size distribution for the LiR-SSR material (Fig. 2a), while LiR-copp material shows an assorted

Table 1 Lattice parameters from Rietveld refinement of LiR-copp and LiR-SSR samples

Lattice parameters	LiR-copp	LiR-SSR
a (Å) ($\pm$ 0.0003)	2.8559	2.8633
c (Å) ($\pm$ 0.003)	14.244	14.268
c/a	4.9875	4.9830

particle-size distribution with larger particle size clusters (Fig. 2b). Also, LiR-copp material presents different particle shapes in contrast with LiR-SSR, which displays agglomerates formed by rounded particles. The variations could be linked to reactant mixing method on each synthesis route and to the process of nucleation and growth of the precursor material $Ni_{0.25}Mn_{0.75}(OH)_2$, which could influence directly in the final particle size of the $Li_{1.2}Ni_{0.2}Mn_{0.6}O_2$ compound [29, 30]. However, in this study, the selected co-precipitated method did not take in consideration the adjustments of the parameter that could play a role in the process of nucleation and growth and, consequently, its influence directly on the final particle size of the materials. Figure 3 shows SEM and EDS images of the LiR-SSR and LiR-copp cathode materials. EDS analysis displays a homogenous distribution of the metals Mn and Ni. In the SEM images, a microstructure in both materials with small size particles can be seen, which facilitates Li^+ intercalation and deintercalation.

FTIR characterization

The spectra of FTIR for LiR-copp and LiR-SSR materials are compared in Fig. 4. The intense peaks at ~500 cm^{-1} are attributed to the M–O (Ni–O and Mn–O) bond vibrations [31], where the intense signal at the lowest wave number (~ 470–500 cm^{-1}) corresponds to the M–O bending vibrations [32] and the following peak (~ 600 cm^{-1}) occurs due to the M–O stretching vibrations [32]. A set of signals corresponding to C-O bonds of remaining CO_3 from the initial precursors ($MnCO_3$, Li_2CO_3) [33] is observed at ~1500 cm^{-1} (related to the asymmetric stretching vibrations) and at ~1130 cm^{-1} (related to the symmetric stretching vibrations) [34]. Both materials do not exhibit a broad band at 3500 cm^{-1}, indicating the absence of -OH groups. Then, it could be inferred that no water remains from the two different synthesis methods, showing that the thermal effect of the treatment was complete by reducing the hydroxylated compounds. As shown in the XRD results, the diffraction patterns of the active materials do not show any phase related to $MnCO_3$ and Li_2CO_3 residues; nonetheless, the X-ray diffraction technique detection limit is only around 2% for mixed materials [35]. The LiR-copp material displays a set of signals of medium intensity located ~862 cm^{-1} that is hardly present in the LiR-SSR, which is related to the bending out of plane vibrations [34] and, also, from CO_3^{2-} residues, in this case, only from the Li_2CO_3. Furthermore, under close analysis, a hardly visible signal at ~730 cm^{-1} for the co-precipitated and the solid-state material can be related to the CO_3 bending in plane vibrations [34]. Additionally, the LiR-copp compound presents a low intensity peak placed ~1025 cm^{-1} and a peak located at ~1600 cm^{-1} that can be attributed to CH_3 rocking vibration and C-O stretching vibration, respectively, in this opportunity from residues

Fig. 2 SEM images of the $Li_{1.2}Ni_{0.2}Mn_{0.6}O_2$ materials synthesized through **a** solid-state reaction and **b** co-precipitation method
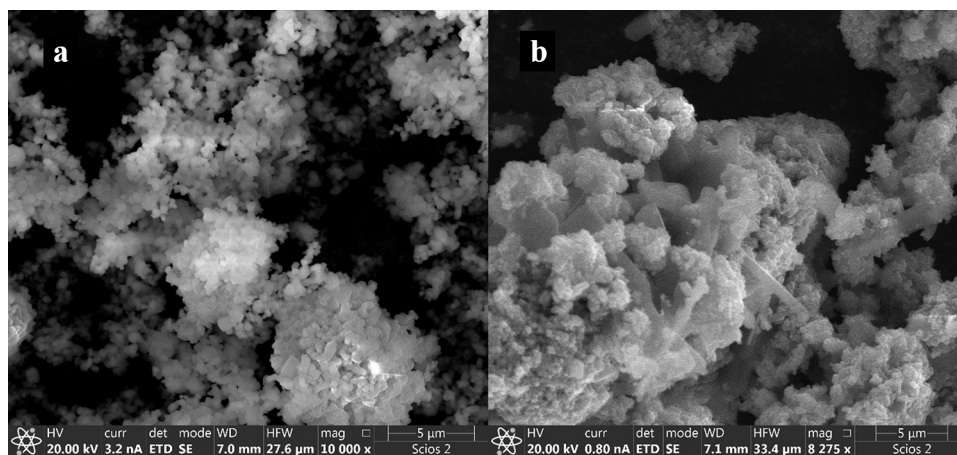
of the acetate groups from the nickel and manganese salts used [36].

Charge–discharge cycling

The cycling performance of the different samples is shown in Fig. 5. The cathodes synthesized by co-precipitation method show an initial discharge capacity of ~200 mAh g^{-1}. However, after a few charge–discharge cycles, a rapid decrease in discharge capacity is observed (around 180 mAh g^{-1}) and, subsequently, a progressive decrease in discharge capacity throughout the 160 cycles, losing 45% of its initial capacity. On the other hand, the initial capacity of LiR-SSR cathode is nearly 150 mAh g^{-1} and after 40 charge–discharge cycles, this sample shows a slight capacity decrease leading to a more stable behavior than that of LiR-copp, retaining most of its original capacity and losing only 16%. The highest values of discharge capacity obtained for LiR-copp materials in the first charge–discharge cycles are in good agreement with

the XRD results, since the bigger interplanar distance in this material facilitates the Li$^+$ intercalation/deintercalation process. However, the results showed a constant decrease in discharge capacity values for this material, in contrast to the behavior of the LiR-SSR material. LiR-SSR delivers lower values in discharge capacity than LiR-copp but almost constant after 160 cycles. This could be associated with the structural variations for LiR-copp samples (as will be shown later in the "Post-cycling analysis" section).

Cyclic voltammetry

Figure 6a and b show the CV curves of the LiR-copp and LiR-SSR electrodes at the first charge–discharge cycle and after 30 cycles, respectively. In both figures, multiple cathodic peaks are observed in the 3.0 to 4.8 V range, which are attributed to Ni and Mn oxidation process. During the first charge–discharge cycle, the co-precipitated material shows a set of two well-defined oxidation peaks around

Fig. 3 SEM images of the $Li_{1.2}Ni_{0.2}Mn_{0.6}O_2$ materials synthesized through **a** solid-state reaction and **d** co-precipitation method. EDS images for Mn and Ni distribution for the LiR-SSR (**b**, **c**) and the LiR-copp (**e**, **f**) samples
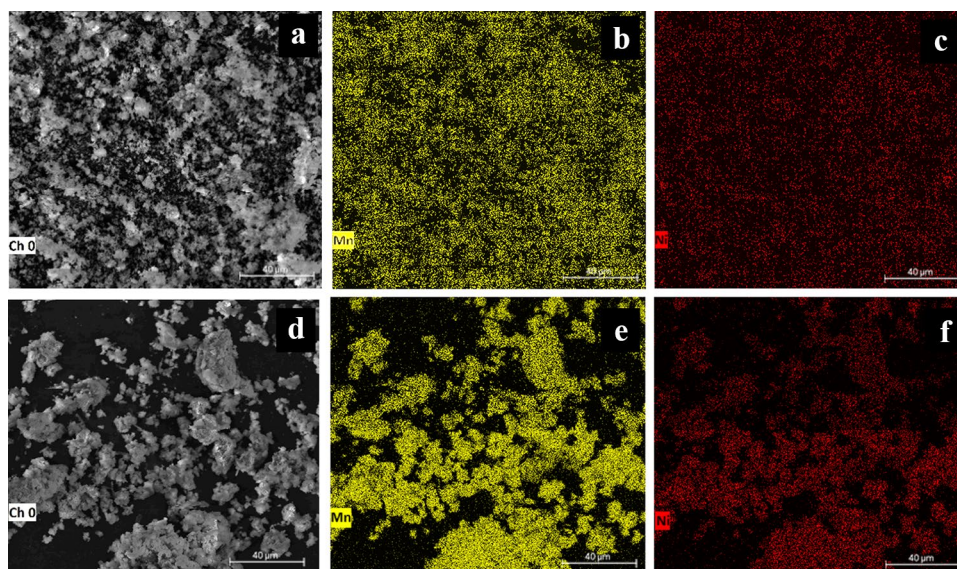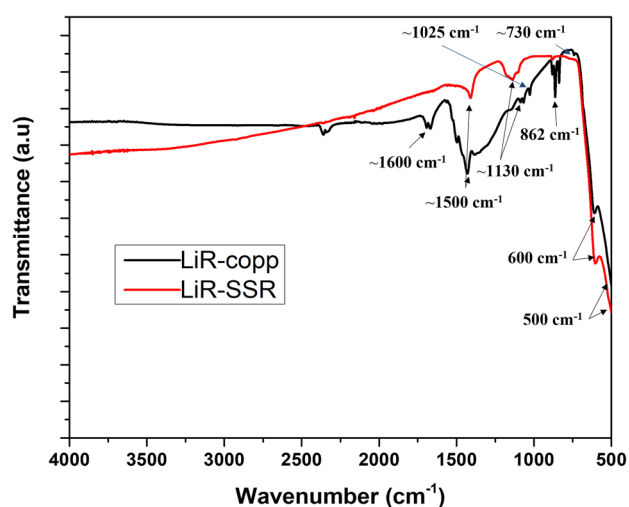
Fig. 4 FTIR of LiR-copp and LiR-SSR materials

3.75 V and 4.25 V, which are related to Ni^{+2}/Ni^{+3} and Ni^{+3}/Ni^{+4} oxidations, respectively [37], while the solid-state reaction material only exhibits a broad peak around 4.25 V that overlaps both oxidation processes. Moreover, both materials show an oxidation peak of low intensity around 3.25 V due to the presence of a certain quantity of Mn^{+3} ions [38] which was expected accordingly to the lattice parameters calculated, mainly for the LiR-SSR materials, where such parameters (a, c) showed higher values. For the material synthesized by co-precipitation, an appreciable increase in current is observed at around 4.7 V in the first cycle, which could be attributed to the irreversible process of Li_2O extraction from Li_2MnO_3 phase to form MnO_2 [39]. This fact could explain the initial high discharge capacity observed in the co-precipitation materials at the first charge–discharge
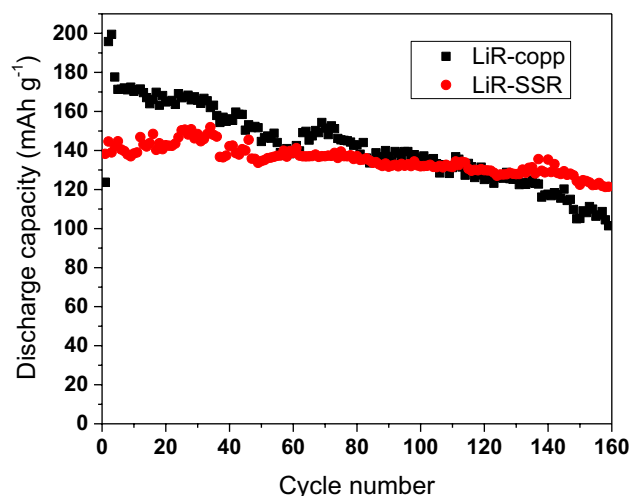

Fig. 5 Cyclic performance of LiR-copp and LiR-SSR electrodes at 0.2 C in the voltage range of 2.0–4.8 V

cycles; nonetheless, this irreversible process is also responsible for a discharge capacity decrease from approximately 200 to 180 mAh g^{-1} (Fig. 5) [40, 41].

After 30 cycles (Fig. 6b), there is no longer any signal related to the Li_2MnO_3 phase activation in both cathodes, although a better definition of all the Ni and Mn oxidation and reduction peaks can be observed. The Ni^{+2}/Ni^{+3} and Ni^{+3}/Ni^{+4} redox couples show a better peak definition and a smaller peak-to-peak voltage interval in the LiR-copp material ($\Delta E_{Ni^{+2}/Ni^{+3}} = 0.27$ V, $\Delta E_{Ni^{+3}/Ni^{+4}} = 0.10$ V against 0.29 V and 0.30 V for the solid-state material, respectively), which indicates how at 30 cycles the co-precipitated material has a higher electrochemical activity and lithium insertion/extraction capacity [42]. This is because the oxidation of Ni^{+2} ions allows Li^+ extraction from the remaining $LiNi_{0.5}Mn_{0.5}O_2$ laminar phase and contributes to the discharge capacity, after the Li_2MnO_3 irreversible phase activation occurred in previous cycles [9, 43]. It is observed that the reduction peak potential related to the redox process Mn^{+4}/Mn^{+3} remains unaltered for LiR-SSR material, while there is an evident displacement to lower potentials in the LiR-copp cathode (Mn^{+4}/Mn^{+3} remains at 3.25 V in the LiR-SSR against a shift to 3.0 V for the LiR-copp); this occurrence is indicative of the formation of a new environment for the Mn^{+4} cations and is usually related to the formation of spinel-like crystal domains upon cycling [28].

In order to determine the presence of the Li_2MnO_3 phase activation peak for the LiR-SSR material, a cyclic voltammetry was carried out using an extended potential range of 2.0 to 5.2 V (Fig. 6c). It can be observed that the Li_2MnO_3 activation appears for this mixed oxide, however, at a potential of ~ 4.9 V, which is located out of the potential range used for the evaluation of the charge–discharge cycling performance. This result further indicates the role of the Li_2MnO_3 activation in the discharge capacity and the stability of the material. This advantageous displacement in potential of the phase activation can be attributed to the higher cationic disorder presented by the LiR-SSR sample, since it is known that in metal transition mixed oxides, the cation disorder yields a higher potential at which the different Li^+ extraction processes occur [44]. The attenuation of this oxidation peak attributable to the Li_2MnO_3 phase in the following cycles (second and third) is an expected phenomenon [8], which differentiates it from signals related to electrolyte decomposition. Further cyclic voltammetry analysis was carried out in the extended potential window (2.0–5.2 V) with a higher concentration electrolyte (1.2 M) with the aim to analyze the possible participation of electrolyte decomposition. These results are presented in Fig. 6d, where the LiR-SSR voltammogram is compared with an aluminum electrode blank, and the oxidation peak is observed located above 4.9 V. In Fig. 6d, it can be observed that the increase of $LiPF_6$ concentration did not suppress the 4.9 V
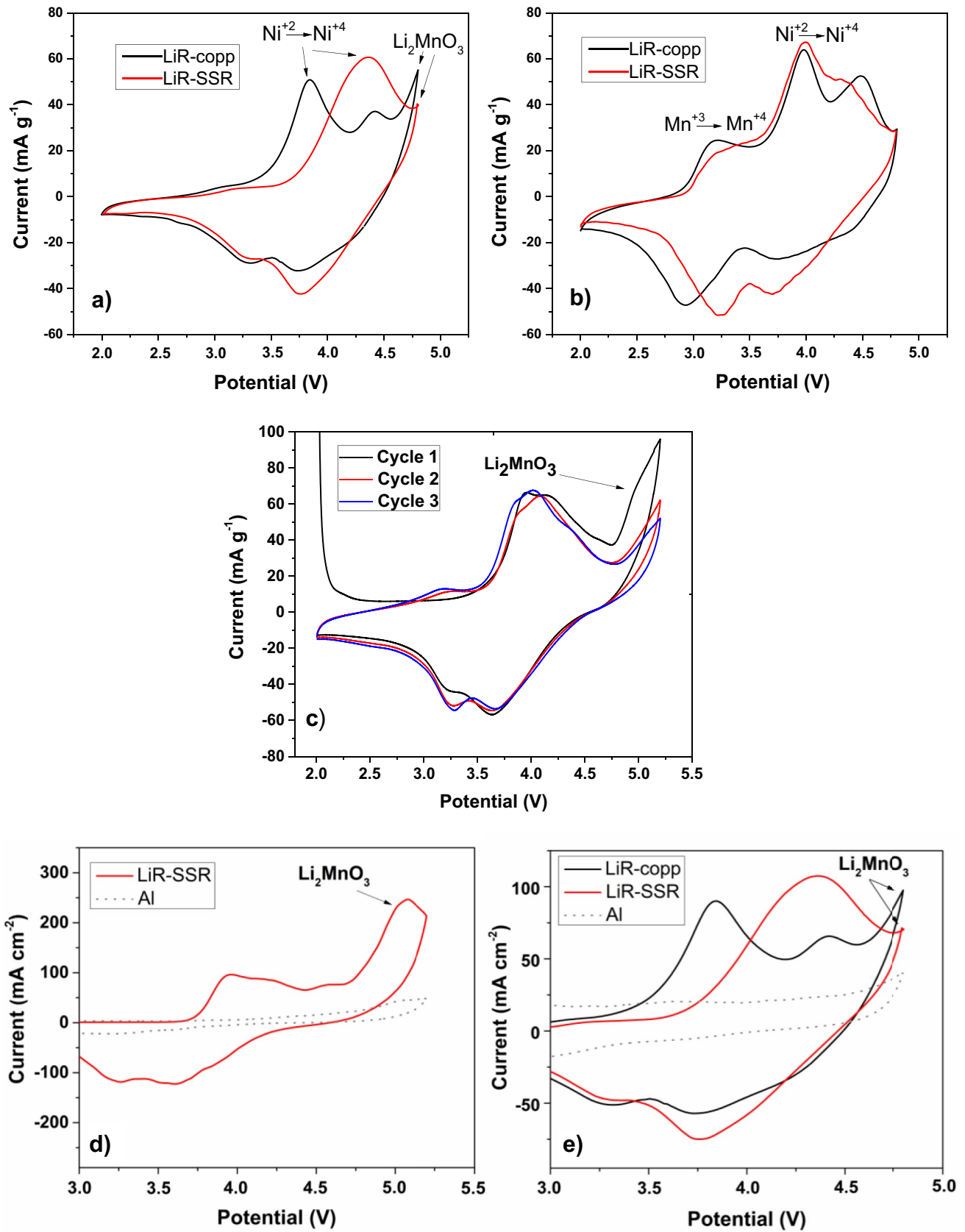
Cyclic voltammograms at 0.1 mVs^{-1} and 2.0–4.8 V, of LiR-copp and LiR-SSR electrodes **a** 1st cycle and **b** after 30 charge–discharge cycles; **c** cyclic voltammograms of LiR-SSR electrodes at first 3 cycles, 2.0–5.2 V; cyclic voltammograms at the first cycle of the LiR materials and an Al electrode **d** in the 2.0–5.2 V range with 1.2 M LiPF$_6$, 1:1 EC: DMC and **e** in the 2.0–4.8 V range with 1 M LiPF$_6$, 1:1 EC: DMC

oxidation peak; in contrast, the Li$_2$MnO$_3$ peak presents a higher relative intensity compared with the 4.0 V Ni^{2+}/Ni^{4+} signal than the same peaks relation in the cyclic voltammetry performed with 1 M electrolyte (Fig. 6c) and the Al blank shows little to none electrolyte decomposition in the voltage range. This evidenced that the high potential signal indeed corresponds primordially to a displaced Li$_2$MnO$_3$ activation signal and its origin cannot be explained just through electrolyte decomposition. Under the initial conditions of electrolyte concentration (1 M LiPF$_6$) in the potential range of 2.0–4.8 V, an Al blank was also performed and compared with the electrochemical responses of both materials (Fig. 6e), where the absence of electrolyte decomposition signal over the Al blank electrode in the area where the Li$_2$MnO$_3$ activation is indicated can be detected.
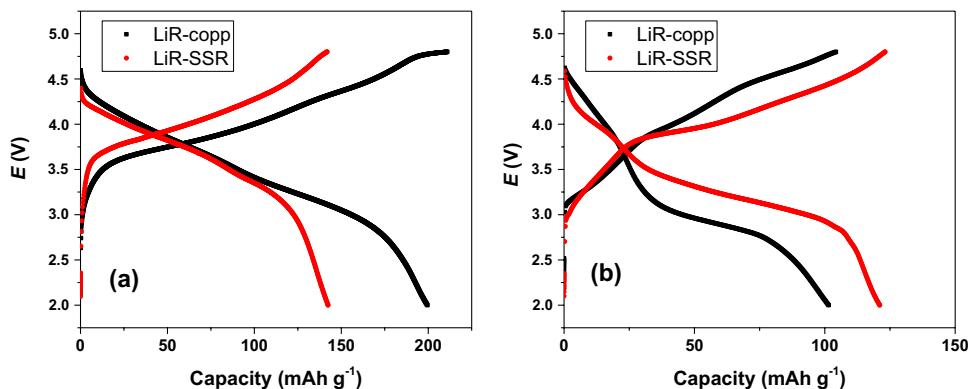
Charge–discharge profiles

Figure 7 shows the charge–discharge profiles at the beginning and at the end of the cycling processes. Initially, for both materials, a plateau around 3.5 V can be observed and is attributable to the Ni^{+2} in the structure, which is oxidized to Ni^{+3} and Ni^{+4}, while Mn keeps its tetravalent state [2, 45]. Additionally, a small plateau can be observed for LiR-copp after 4.5 V, which is characteristic of the Li$_2$MnO$_3$ activation, and this may also explain the extra discharge capacity of the material [41, 46]. After the cycling process, voltage decay can be observed especially for the co-precipitated material. This phenomenon is usually explained through a phase-transition-voltage-decay mechanism from a laminar to a spinel phase. This mechanism occurs due to a greater Li$^+$ extraction upon charging to 4.8 V and the Li an O irreversible removal after the Li$_2$MnO$_3$ activation. Both processes

generate vacant sites where the transition metal cations can migrate, giving rise to the formation of the new spinel phase [47–49]. The newly formed spinel phases are known to be prone to Jahn–Teller distortion in which the Mn^{+3} to Mn^{+4} ratios suffer variations upon electrochemical cycling. This behavior modifies the crystal distribution and the three-dimensional Li$^+$ diffusion pathways causing the capacity and voltage fade, as it was observed in the Li-copp material after its Li$_2$MnO$_3$ activation [50]. Likewise, the cyclic voltammograms performed after 30 cycles indicated possible formation of spinel phase domains evidenced by a potential shift to lower potential of the Mn^{+4}/Mn^{+3} redox process [28]. It is also reported that after the layered to spinel phase transition happens, the Mn^{+3} is likely to undergo a disproportionate reaction that produces Mn^{+2} which is soluble in the electrolyte and allows the loss of active material [51].

Rate capability

Figure 8 shows the rate performance for the LiR-copp and LiR-SSR materials. Cells with both materials were tested from 0.2 to 10 C between voltage limits of 2–4.8 V, repeating five charge–discharge cycles for each C-rate. It is noticeable that the discharge capacity of both samples decreases considerably when a higher rate is applied; however, the co-precipitated material shows almost no discharge capacity at 5 C and 10 C. Furthermore, the LiR-SSR material recovers 97% of its original capacity, while LiR-copp does not retain its capacity at 0.2 C in the second round and the cell loses its entire function. These results show the highest stability of the lithium-rich oxide for the materials obtained through the solid-state reaction thanks to the lack of Li$_2$MnO$_3$ activation in the cycling conditions applied during the rate capability determination for this material. It is well-reported that the Li$_2$MnO$_3$ phase is responsible for the deficient rate in other Li-Rich samples [52], and the possible formation of spinel phases at higher current rates generates greater Mn^{+3}-rich areas that further create Jahn–Teller distortion [50] hindering the electrochemical performance until the cathode no longer presents operability.

Fig. 7 *E* vs. charge–discharge capacity profiles for both electrodes: **a** first cycle and **b** after 160 cycles
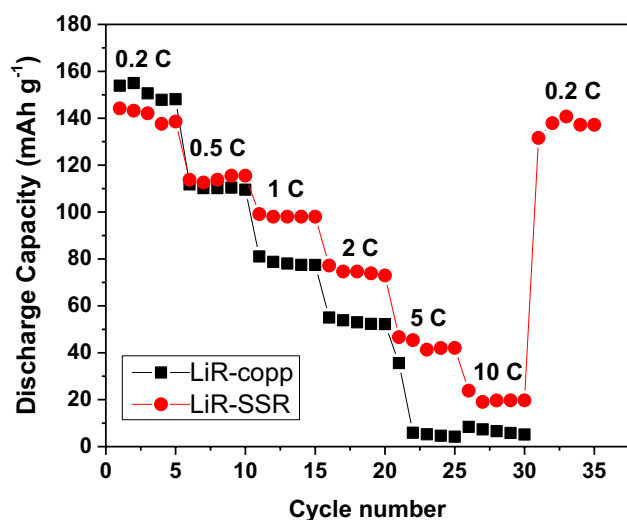
Fig. 8 Rate capability of LiR-copp and LiR-SSR electrodes

Charge–discharge cycling with variations in the potential range

As seen from Fig. 6c, the Li_2MnO_3 phase activation for the LiR-SSR seems to occur at a higher potential than regular, so the cycling performance for this cathode was also determined using a wider potential range: 2.0–5.2 V, and the results obtained were compared to previously using the range up to 4.8 V (Fig. 9a). It is remarkable that forcing the phase activation by using a higher polarization, the solid-state reaction compound shows similar behavior to the charge–discharge cycling of the LiR-coop material: in the range of 2–4.8 V (Fig. 5). That is, an initial discharge capacity higher than 200 mAh g^{-1} and a poor stability that generates a rapid drop in the capacity during the cycling. This shows the importance of the Li_2MnO_3 phase activation to produce higher capacities. However, as was previously
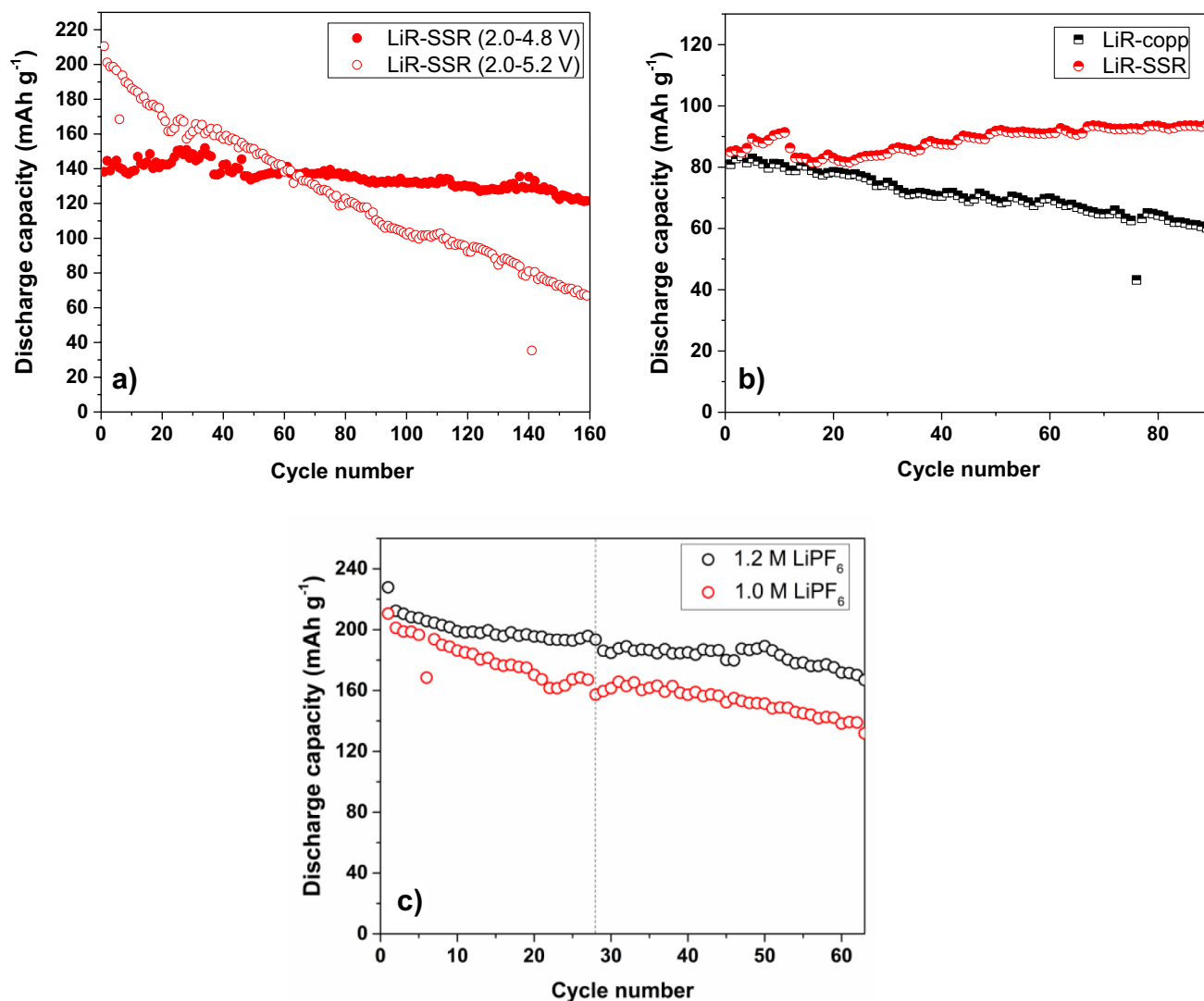

Fig. 9 Cyclic performance of **a** LiR-SSR material at 0.2 C, 2.0–4.8 V, and 2.0–5.2 V. **b** LiR-copp and LiR-SSR electrodes at 0.5 C, between 2.0–4.5 V. **c** LiR-SSR material at 0.2 C in the 2.0–5.2 V range, with 1 M and 1.2 M electrolyte concentrations

described, it decreases the stability. Additionally, 100 charge–discharge cycles (0.5 C) were carried for both materials reducing the range potential to 2.0–4.5 V with aims of avoiding or diminishing the Li_2MnO_3 phase activation (Fig. 9b). The lower discharge capacities are the results of the use of a higher C rate for the cycling process. Under these conditions, the LiR-SSR cathode shows a growing tendency in its capacity until stabilizing during the last 40 cycles. On the other hand, and despite the fact that the LiR-coop remains with a slight capacity fade, the initial abrupt capacity drop observed when cycling from 2.0 to 4.8 V is not displayed. Furthermore, the total capacity fade observed during the 100 cycles represents only 27% of the initial capacity against the total loss of 34% during the first 100 cycles using the range potential up to 4.8 V (Fig. 5).

The galvanostatic charge and discharge cycling was tested for the LiR-SSR material using the extended potential range of 2.0–5.2 V and a higher concentration electrolyte (1.2 M in order to evaluate the role of electrolyte decomposition in the stability of the cathodes) (Fig. 9c). The initial discharge capacity of the LiR-SSR material with the 1.2 M electrolyte was increased to 230 mAh g^{-1} in the first cycle and an improvement in stability was observed. However, after 28 cycles (vertical line in Fig. 9c), both conditions developed a capacity fade with the same decreasing slope. Once more, these results indicate that the process of the Li_2MnO_3

activation contributes more to the capacity decrease than the partial electrolyte decomposition.

Electrochemical impedance spectroscopy

Electrochemical impedance spectroscopy was performed to analyze the difference in the electrochemical performance of LiR-copp and LiR-SSR electrodes. The measured impedance spectra of the two samples after 20 charge–discharge cycles at the state of charge (SOC) of 50% are presented in Fig. 10a. EIS plots show well-defined zones made up of two semicircles and a low-frequency tail. The low-frequency tail is expected to have an angle of 45°; however, a lower angle can be observed due to surface roughness and other factors [53]. One of the semicircles is in the high-frequency region (as observed in the enlarged inserted graph) and the other is located in the middle-frequency region, as shown in Fig. 10a. The high-frequency semicircle (with characteristic frequencies of 502 Hz and 1000 Hz for the LiR-SSR and the LiR-copp materials, respectively) can be attributed to the impedance of Li^+ migration across the SEI film [54, 55]. The semicircle in the middle-frequency region (with characteristic frequencies of 0.0125 Hz and 0.0398 Hz for the LiR-SSR and LiR-copp accordingly) is related to the impedance of charge transfer, and the low-frequency tail is the impedance of Li-ion migration in the cathode material

Fig. 10 **a** Nyquist plots of LiR-copp and LiR-SSR samples and the correlatively magnified EIS profile in the range of 0–85 Ω to show the high-frequency zone. **b** Equivalent circuit used to fit the measured impedance spectra
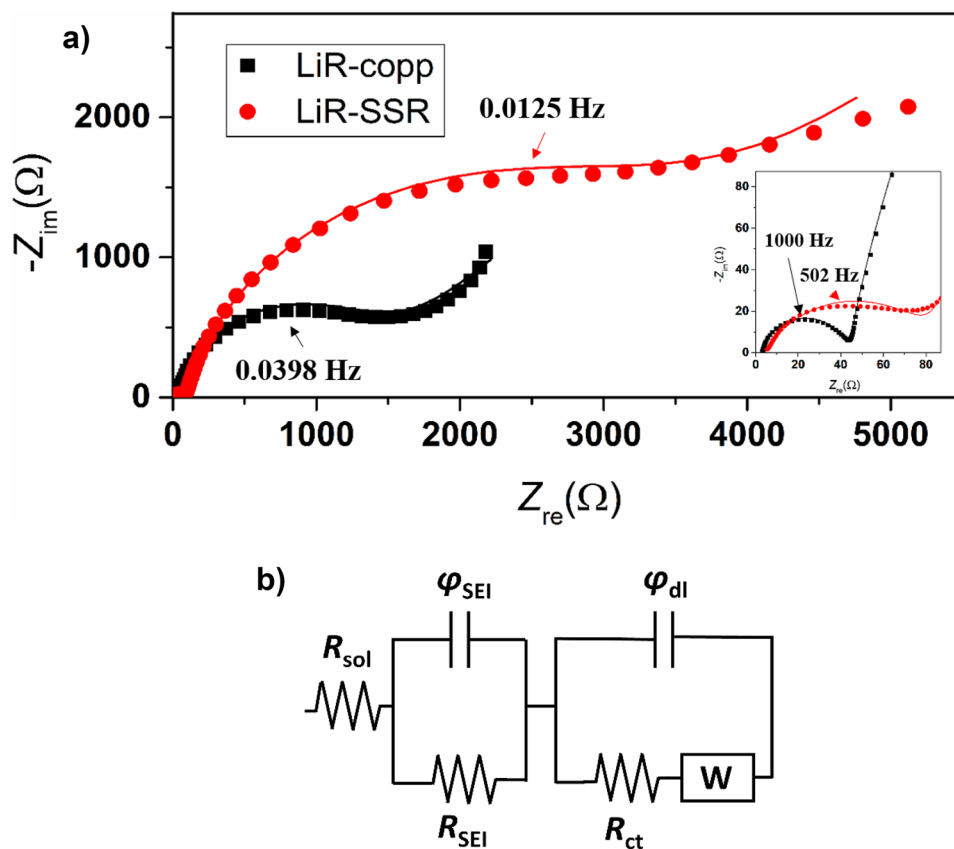
Table 2 Fitting values of R_{ct} and R_{SEI} for both cathode materials using the equivalent circuit shown in Fig. 10b

Parameter	LiR-copp	LiR-SSR
R_{SEI} (Ω)	3.05 ± 0,05	79 ± 1
R_{ct} (Ω)	1370 ± 30	3500 ± 100
Goodness of fit	4.70 10^{-4}	1.210 10^{-3}

[56]. A larger diameter is associated with a greater impedance [57]. Accordingly, it could be affirmed that the compound obtained by co-precipitation process presents a lower resistance to Li$^+$ migration through the SEI film and lower resistance to the charge transfer at 20 cycles.

The experimental data were fitted using the equivalent circuit shown in Fig. 10b. The fitted impedance parameters of the equivalent circuit are listed in Table 2, where R_{ct} is the cathode charge transfer resistance and R_{SEI} is the cathode migration across the SEI film resistance. For the co-precipitated cathode material, both magnitudes represent lower impedances compared to the material synthesized by solid-state reaction (R_{SEI} = 3.05 Ω against 79 Ω and R_{ct} = 1370 Ω against 3500 Ω). The semicircle in the middle-frequency region is related to the charge transfer impedance, which is associated with Li$^+$ extraction reaction throughout the Ni^{+2} cation oxidation [9, 43].

This result, along with that observed by cyclic voltammetry (Fig. 6b), corresponds to the behavior observed in the discharge capacity of both cathodes at 20 cycles, where the co-precipitated material still has a higher discharge capacity than LiR-SSR (Fig. 5).

Post-cycling analysis

Figure 11a shows the Nyquist plots for the cathode materials at the state of charge (SOC) of 50%, after performing 100 cycles at 0.5 C between 2.0 and 4.8 V. The semicircles in high and middle frequency zone are still present as shown in Fig. 11c, with characteristic frequencies of 5034 Hz and 0.0316 Hz, respectively, for the LiR-SSR loops. In the case of LiR-copp cathode, the greater magnitude of the impedance does not allow to observe the low frequency line and is only visible an incomplete middle frequency loop and the high frequency EIS-related loop (characteristic frequency of 790 Hz). These results show that the high frequency semicircle related to the SEI formation and the semicircle related to the charge transfer for the LiR-coop are greater than the ones for the LiR-SSR. This interchange in the EIS behavior compared to the Nyquist plots obtained at 20 cycles was expected since the discharge capacities at 100 cycles of the solid-state material are higher than the capacity of the co-precipitated one in the potential range analyzed (Fig. 11b). This indicates the direct relationship between the impedance results with the discharge capacities for synthesized materials.

Figure 12a shows the XRD spectra of the pristine and cycled cathode materials where a "shoulder like" signal located between 44 and 45°, adjacent to the (104) peak from

Fig. 11 **a** Nyquist plots of LiR-copp and LiR-SSR samples after 100 cycles, **b** the last 20 cycles before performing EIS, and **c** enlarged EIS zone at high and medium frequency
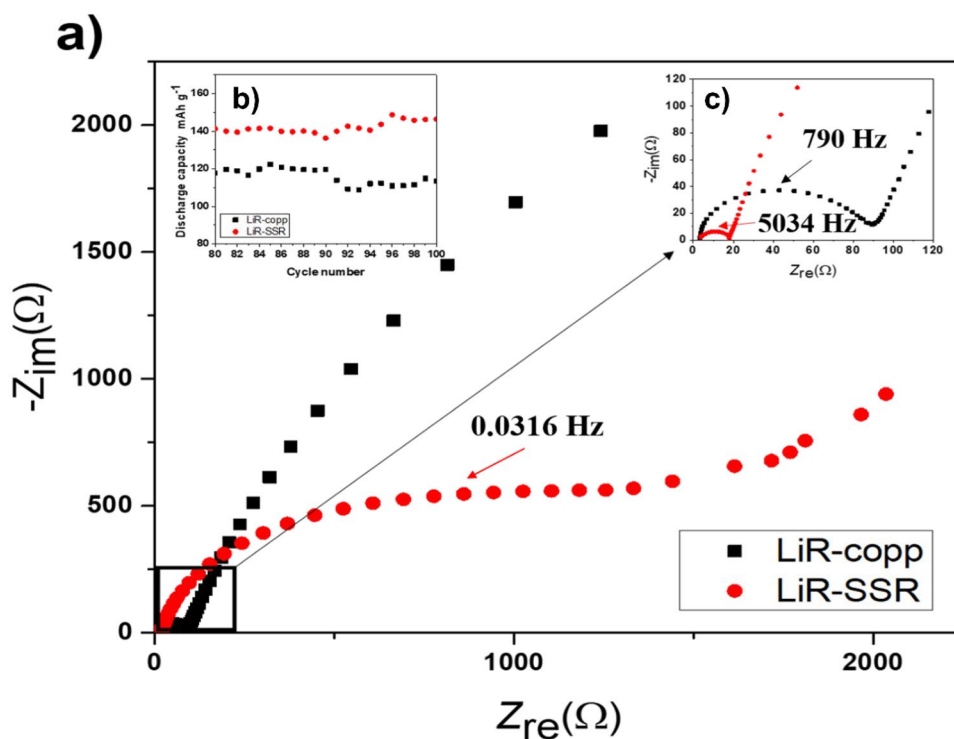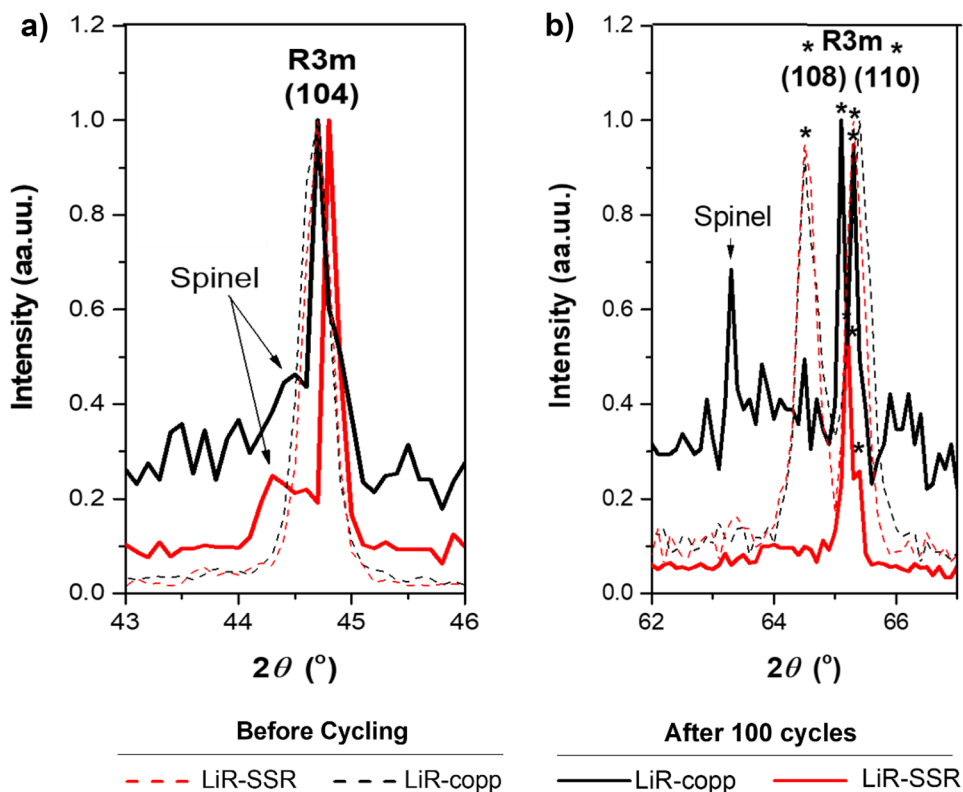
Fig. 12 XRD spectra of the cathodes **a** in the 43 to 46° 2 Θ range and **b** in the 62 to 67° 2 Θ range

the laminar phase $LiMO_2$, points to the presence of spinel-like crystal domains (plane (400)) [58, 59]. The higher intensity of this signal in the LiR-copp materials indicates a higher amount of the spinel phase. Also, in the range comprised between 62 and 67° (Fig. 12b), a low diffraction peak (detected using the criteria of signal to noise ratio >3) located before the (108) and (110) planes of the cycled LiR-copp materials can also be attributed to the presence of a spinel-like phase (plane (440) [59]) [60]. This agrees with the above descriptions mentioned about the phase transition which causes a more pronounced voltage fade in the co-precipitated materials. It shows, once more, that the layered to spinel phase conversion observed when cycling for 2.0 to 4.8 V for the LiR-copp electrodes is related to the Li_2MnO_3 activation in this material (which does not occur in the LiR-SSR materials since the activation happens at higher potentials) and, at the same time, this phase evolution is also related not only to the voltage fade but also to the capacity and cyclability fade [61], both observed in galvanostatic cycling behavior and rate capability (Figs. 5 and 8, respectively).

Conclusions

Lithium-rich materials with $Li_{1.2}Ni_{0.2}Mn_{0.6}O_2$ composition were successfully synthesized by two methods: co-precipitation and solid-state reaction. By XRD, it was observed that both

materials have the typical signals of this lithium-rich material and show good crystallinity. By SEM and EDS analyses, a homogeneous distribution of Mn and Ni was observed in both materials, as well as a laminar particle structure and a small particle size that enable the intercalation and deintercalation of Li^+. In addition, the typical lithium-rich material bond bands were seen by FTIR-ATR.

The materials synthesized by co-precipitation method deliver an initial discharge capacity of around 200 mAh g^{-1}; however, this capacity drops quickly on cycling. This behavior is related to the activation of Li_2MnO_3 which also generates in the cycling beginning, in the potential range of 2.0–4.8 V, the initial extra capacity mainly observed in the co-precipitated material. On the other hand, LiR-SSR material delivers an initial discharge capacity lower than that of LiR-copp material, but it remains fairly stable throughout cycling; this could be related to the absence of the Li_2MnO_3 phase activation, which, for LiR-SSR material, occurs at potentials located above the regular range of potentials used for lithium-rich mixed oxides. This potential shift could be due to higher cation disorder present in the LiR-SSR sample. Also, the rate performance of LiR-SSR materials shows that it recovers 97% of its original capacity after cycling to 10 C, in contrast to LiR-copp materials which do not retain its capacity, and cell operation cannot be restored. From the impedance measurements in the high-frequency zone, it can be seen that the compound obtained by co-precipitation

process presents a lower resistance to Li $^+$ migration through the SEI film and charge transfer at the beginning of cycling than the solid-state reaction material. This could be related to the observed discharge capacities since after 100 cycles the impedance reverses its behavior as it does during the cycling.

From these results, we conclude that the cyclability and rate capability performance of lithium-rich materials strongly depend on the synthesis procedure. Even using the same elemental stoichiometric proportions, different structural characteristics can be achieved that allow a potential shift at which the Li_2MnO_3 activation occurs. If this phenomenon is partially or completely avoided, it would also lead to the suppression of the layered to spinel phase conversion that, eventually, would produce the voltage and capacity fade, and with this, an improvement in the stability, rate capability, and electrochemical behavior would be obtained.

In terms of electrochemical performance, the results in the first cycles were better for the materials synthesized by co-precipitation, though materials with greater stability were obtained by the solid-state reaction method, not only in the first cycles, but in the 160 charge–discharge cycles evaluated. Therefore, the solid-state reaction represents a method to synthesize electrochemical well-performing Li-rich materials when used under suitable cycling conditions. The advantage is that it is a simple method for large-scale synthesis that allows to rapidly perform the modifications required in chemical composition and physical structural characteristics.

References

1. Scrosati B, Garche J (2010) Lithium batteries: status, prospects and future. J Power Sources 195:2419–2430. https://doi.org/10.1016/j.jpowsour.2009.11.048
2. Xiang X, Li W (2015) Facile synthesis of lithium-rich layered oxide Li[Li0.2Ni0.2Mn0.6]O2 as cathode of lithium-ion batteries with improved cyclic performance. J Solid State Electrochem 19:221–227. https://doi.org/10.1007/s10008-014-2590-0
3. Dou S (2013) Review and prospect of layered lithium nickel manganese oxide as cathode materials for Li-ion batteries. J Solid State Electrochem 17:911–926. https://doi.org/10.1007/s10008-012-1977-z
4. Placke T, Kloepsch R, Dühnen S, Winter M (2017) Lithium ion, lithium metal, and alternative rechargeable battery technologies: the odyssey for high energy density. J Solid State Electrochem 21:1939–1964. https://doi.org/10.1007/s10008-017-3610-7
5. Diouf B, Pode R (2015) Potential of lithium-ion batteries in renewable energy. Renew Energy 76:375–380. https://doi.org/10.1016/j.renene.2014.11.058
6. Liu Q, Su X, Lei D et al (2018) Approaching the capacity limit of lithium cobalt oxide in lithium ion batteries via lanthanum and aluminium doping. Nat Energy 3:936–943. https://doi.org/10.1038/s41560-018-0180-6
7. Li M, Wang H, Zhao L et al (2019) Improving the electrochemical performance of lithium-rich oxide layer material with Mg and La co-doping. J Alloys Compd 782:451–460. https://doi.org/10.1016/j.jallcom.2018.12.072
8. Pan H, Zhang S, Chen J et al (2018) Li- and Mn-rich layered oxide cathode materials for lithium-ion batteries: a review from fundamentals to research progress and applications. Mol Syst Des Eng 3:748–803. https://doi.org/10.1039/C8ME00025E
9. Gu R-M, Yan S-Y, Sun S et al (2015) Electrochemical behavior of lithium-rich layered oxide Li[Li0.23Ni0.15Mn0.62]O2 cathode material for lithium-ion battery. J Solid State Electrochem 19:1659–1669. https://doi.org/10.1007/s10008-015-2796-9
10. Qing R-P, Shi J-L, Xiao D-D et al (2016) Cathode materials: enhancing the kinetics of Li-rich cathode materials through the pinning effects of gradient surface Na$^+$ doping (Adv. Energy Mater. 6/2016). Adv Energy Mater 6. https://doi.org/10.1002/aenm.201670035
11. Lu C, Wu H, Zhang Y et al (2014) Cerium fluoride coated layered oxide Li1.2Mn0.54Ni0.13Co0.13O2 as cathode materials with improved electrochemical performance for lithium ion batteries. J Power Sources 267:682–691. https://doi.org/10.1016/j.jpowsour.2014.05.122
12. Watanabe A, Yamamoto K, Uchiyama T et al (2020) Capacity improvement by nitrogen doping to lithium-rich cathode materials with stabilization effect of oxide ions redox. ACS Appl Energy Mater 3:4162–4167. https://doi.org/10.1021/acsaem.0c00564
13. Zhang K, Sheng H, Wu X et al (2020) Improving electrochemical properties by sodium doping for lithium-rich layered oxides. ACS Appl Energy Mater 3:8953–8959. https://doi.org/10.1021/acsaem.0c01402
14. Zhang J, Lu Q, Fang J et al (2014) Polyimide encapsulated lithium-rich cathode material for high voltage lithium-ion battery. ACS Appl Mater Interfaces 6:17965–17973. https://doi.org/10.1021/am504796n
15. He W, Qian J, Cao Y et al (2012) Improved electrochemical performances of nanocrystalline Li[Li0.2Mn0.54Ni0.13Co0.13]O2 cathode material for Li-ion batteries. RSC Adv 2:3423–3429. https://doi.org/10.1039/C2RA20122D
16. Koga H, Croguennec L, Ménétrier M et al (2013) Reversible oxygen participation to the redox processes revealed for Li1.20Mn0.54Co0.13Ni0.13O2. J Electrochem Soc 160:A786. https://doi.org/10.1149/2.038306jes
17. Liu Y, Wang Q, Zhang Z et al (2016) Investigation the electrochemical performance of layered cathode material Li 1.2 Ni 0.2 Mn 0.6 O 2 coated with Li 4 Ti 5 O 12. Adv Powder Technol 27:1481–1487. https://doi.org/10.1016/j.apt.2016.05.008
18. Xu J, Sun M, Qiao R et al (2018) Elucidating anionic oxygen activity in lithium-rich layered oxides. Nat Commun 9:947. https://doi.org/10.1038/s41467-018-03403-9
19. Hamad KI, Xing Y (2019) Stabilizing Li-rich NMC materials by using precursor salts with acetate and nitrate anions for Li-ion batteries. Batteries 5:69. https://doi.org/10.3390/batteries5040069
20. Hu S, AnoopS P, Liang G et al (2019) Li-rich layered oxides and their practical challenges: recent progress and perspectives. Electrochem Energy Rev 2:277–311. https://doi.org/10.1007/s41918-019-00032-8
21. Song X, Huang H, Zhong W (2019) Sucrose-assisted synthesis of layered lithium-rich oxide Li[Li0.2Mn0.56Ni0.16Co0.08]O2 as a cathode of lithium-ion battery. Crystals 9:436. https://doi.org/10.3390/cryst9090436
22. Ohzuku T, Ueda A, Nagayama M (1993) Electrochemistry and structural chemistry of LiNiO2 (R3m) for 4 volt secondary lithium cells. J Electrochem Soc 140:1862–1870. https://doi.org/10.1149/1.2220730

23. An J, Shi L, Chen G et al (2017) Insights into the stable layered structure of a Li-rich cathode material for lithium-ion batteries. J Mater Chem A 5:19738–19744. https://doi.org/10.1039/C7TA05971J

24. Lu Z, Beaulieu LY, Donaberger RA et al (2002) Synthesis, structure, and electrochemical behavior of Li [Ni x Li1 / 3–2x / 3Mn2 / 3–x / 3] O 2. J Electrochem Soc 149:A778. https://doi.org/10.1149/1.1471541

25. Ates MN, Mukerjee S, Abraham KM (2015) A high rate Li-rich layered MNC cathode material for lithium-ion batteries. RSC Adv 5:27375–27386. https://doi.org/10.1039/C4RA17235C

26. He X, Wang J, Wang L, Li J (2016) Nano-crystalline Li1.2Mn0.6Ni0.2O2 prepared via amorphous complex precursor and its electrochemical performances as cathode material for lithium-ion batteries. Materials 9:661. https://doi.org/10.3390/ma9080661

27. Abdel-Ghany A, Hashem AM, Mauger A, Julien CM (2020) Lithium-rich cobalt-free manganese-based layered cathode materials for Li-ion batteries: suppressing the voltage fading. Energies 13:3487. https://doi.org/10.3390/en13133487

28. Wang C-C, Lin Y-C, Chou P-H (2015) Mitigation of layer to spinel conversion of a lithium-rich layered oxide cathode by substitution of Al in a lithium ion battery. RSC Adv 5:68919–68928. https://doi.org/10.1039/C5RA11665A

29. Li Y, Li Z, Chen C et al (2021) Recent progress in Li and Mn rich layered oxide cathodes for Li-ion batteries. J Energy Chem 61:368–385. https://doi.org/10.1016/j.jechem.2021.01.034

30. Yu F-D, Que L-F, Wang Z-B et al (2017) Controllable synthesis of hierarchical ball-in-ball hollow microspheres for a high performance layered Li-rich oxide cathode material. J Mater Chem A 5:9365–9376. https://doi.org/10.1039/C7TA02553J

31. A.Said AE-A, El-Wahab MMA, Soliman SA, Goda MN (2014) Synthesis and characterization of nano CuO-NiO mixed oxides. Nanosci Nanoeng 2:17–28. https://doi.org/10.13189/nn.2014.020103

32. Stella C, Soundararajan N, Ramachandran K (2014) Structural, optical, dielectric and magnetic properties of Mn1−xCoxO2 nanowires. Superlattices Microstruct 71:203–210. https://doi.org/10.1016/j.spmi.2014.03.044

33. Bizeau J, Tapeinos C, Marella C et al (2017) Synthesis and characterization of hyaluronic acid coated manganese dioxide microparticles that act as ROS scavengers. Colloids Surf B Biointerfaces 159:30–38. https://doi.org/10.1016/j.colsurfb.2017.07.081

34. Pasierb P, Komornicki S, Rokita M, Rękas M (2001) Structural properties of Li2CO3–BaCO3 system derived from IR and Raman spectroscopy. J Mol Struct 596:151–156. https://doi.org/10.1016/S0022-2860(01)00703-7

35. Bunaciu AA, Udriştioiu EG, Aboul-Enein HY (2015) X-ray diffraction: instrumentation and applications. Crit Rev Anal Chem 45:289–299. https://doi.org/10.1080/10408347.2014.949616

36. Ito K, Bernstein HJ (1956) The vibrational spectra of the formate, acetate, and oxalate ions. Can J Chem 34:170–178. https://doi.org/10.1139/v56-021

37. Li J, Zhan C, Lu J et al (2015) Improve first-cycle efficiency and rate performance of layered-layered Li1.2Mn0.6Ni0.2O2 using oxygen stabilizing dopant. ACS Appl Mater Interfaces 7:16040–16045. https://doi.org/10.1021/acsami.5b04343

38. Uzun D (2015) Boron-doped Li1.2Mn0.6Ni0.2O2 as a cathode active material for lithium ion battery. Solid State Ion 281:73–81. https://doi.org/10.1016/j.ssi.2015.09.008

39. Yang C-C, Liao P-C, Wu Y-S, Lue SJ (2017) Electrochemical performance of Li-rich oxide composite material coated with Li0.75La0.42TiO3 ionic conductor. Appl Surf Sci 399:670–681. https://doi.org/10.1016/j.apsusc.2016.12.121

40. Chen H, Islam MS (2016) Lithium extraction mechanism in Li-Rich Li2MnO3 involving oxygen hole formation and dimerization. Chem Mater 28:6656–6663. https://doi.org/10.1021/acs.chemmater.6b02870

41. Mezaal MA, Qu L, Li G et al (2017) LiMO2@Li2MnO3 positive-electrode material for high energy density lithium ion batteries. J Solid State Electrochem 21:145–152. https://doi.org/10.1007/s10008-016-3345-x

42. Hu J-P, Sheng H, Deng Q et al (2020) High-rate layered cathode of lithium-ion batteries through regulating three-dimensional agglomerated structure. Energies 13:1602. https://doi.org/10.3390/en13071602

43. Zhao S, Yan K, Zhang J et al (2021) Reaction mechanisms of layered lithium-rich cathode materials for high-energy lithium-ion batteries. Angew Chem Int Ed 60:2208–2220. https://doi.org/10.1002/anie.202000262

44. Abdellahi A, Urban A, Dacek S, Ceder G (2016) Understanding the effect of cation disorder on the voltage profile of lithium transition-metal oxides. Chem Mater 28:5373–5383. https://doi.org/10.1021/acs.chemmater.6b01438

45. Li L, Lee KS, Lu L (2014) Li -rich layer-structured cathode materials for high energy Li -ion batteries. Funct Mater Lett 07:1430002. https://doi.org/10.1142/S1793604714300023

46. Zhang X, Meng X, Elam JW, Belharouak I (2014) Electrochemical characterization of voltage fade of Li1.2Ni0.2Mn0.6O2 cathode. Solid State Ion 268:231–235. https://doi.org/10.1016/j.ssi.2013.09.052

47. Kim D, Sandi G, Croy JR et al (2013) Composite 'Layered-Layered-Spinel' cathode structures for lithium-ion batteries. J Electrochem Soc 160:A31–A38. https://doi.org/10.1149/2.049301jes

48. Boulineau A, Simonin L, Colin J-F et al (2013) First evidence of manganese–nickel segregation and densification upon cycling in Li-rich layered oxides for lithium batteries. Nano Lett 13:3857–3863. https://doi.org/10.1021/nl4019275

49. Xie H, Cui J, Yao Z et al (2022) Revealing the role of spinel phase on Li-rich layered oxides: a review. Chem Eng J 427:131978. https://doi.org/10.1016/j.cej.2021.131978

50. Li X, Xu Y, Wang C (2009) Suppression of Jahn-Teller distortion of spinel LiMn2O4 cathode. J Alloys Compd 479:310–313. https://doi.org/10.1016/j.jallcom.2008.12.081

51. Yang Z, Zheng C, Wei Z et al (2022) Multi-dimensional correlation of layered Li-rich Mn-based cathode materials. Energy Mater. https://doi.org/10.20517/energymater.2022.02

52. Xiong L, Sun M, Xu Y et al (2018) Synthesis of carbon coated Li2MnO3 cathode material with enhanced rate capability for lithium-ion batteries. Solid State Ion 325:170–175. https://doi.org/10.1016/j.ssi.2018.08.008

53. Zhang Y, Liu Z, Wang Z et al (2019) Electrochemical impedance spectroscopy study of lithium-rich material 0.5Li2MnO3·0.5LiNi1/3Co1/3Mn1/3O2 in the first two charge-discharge cycles. Electrochim Acta 310:136–145. https://doi.org/10.1016/j.electacta.2019.04.112

54. Liu Y, Lv J, Liu S et al (2013) Improved electrochemical performance of Li1.2Ni0.2Mn0.6O2 cathode materials by ball milling and carbon coating. Powder Technol 239:461–466. https://doi.org/10.1016/j.powtec.2013.02.039

55. He W, Zheng H, Ju X et al (2017) Multistage Li 1.2 Ni 0.2 Mn 0.6 O 2 micro-architecture towards high-performance cathode materials for lithium-ion batteries. Chem Electro Chem 4:3250–3256. https://doi.org/10.1002/celc.201700727

56. Lu Y, Pang M, Shi S et al (2018) Enhanced electrochemical properties of Zr4+-doped Li1.20[Mn0.52Ni0.20Co0.08]O2 cathode material for lithium-ion battery at elevated temperature. Sci Rep 8:2981. https://doi.org/10.1038/s41598-018-21345-6

57. Chen Y, Wang X, Zhang J et al (2019) Al 2 O 3 -coated Li 1.2 Mn 0.54 Ni 0.13 Co 0.13 O 2 nanotubes as cathode materials for high-performance lithium-ion batteries. RSC Adv 9:2172–2179. https://doi.org/10.1039/C8RA09428D

58. Zhao T, Zhou N, Zhang X et al (2017) Structure evolution from layered to spinel during synthetic control and cycling process of

Fe-containing Li-rich cathode materials for lithium-ion batteries. ACS Omega 2:5601–5610. https://doi.org/10.1021/acsomega.7b00689

59. Fu P, Lu W, Lei W et al (2013) Thermal stability and microstructure characterization of MgAl2O4 nanoparticles synthesized by reverse microemulsion method. Mater Res 16:844–849. https://doi.org/10.1590/S1516-14392013005000062

60. Hou XL, Huang JT, Hu ZH et al (2018) Molten salt synthesis and formation mechanism of plate-like $MgAl_2O_4$ spinel. Solid State Phenom 281:278–284. https://doi.org/10.4028/www.scientific.net/SSP.281.278

61. Shimoda K, Oishi M, Matsunaga T et al (2017) Direct observation of layered-to-spinel phase transformation in Li_2MnO_3 and the spinel structure stabilised after the activation process. J Mater Chem A 5:6695–6707. https://doi.org/10.1039/C6TA11151C